

A study on Parasite-Effect with Strapdown-Seeker in Consideration of Time-Delay

Ju-Hyeon Hong*

Cranfield University, Collage Road, Cranfield, MK43 0AL, United Kingdom

Sang-Sup Park†

Lumir Inc., 767 Sinsuro, Yonginsi, Kyunggido, 16827, Republic of Korea

Chang-Hun Lee‡

Korea Advanced Institute of Science and Technology (KAIST), Daejeon, 34141, Repblic of Korea

Chang-Kyung Ryoo§

Inha University, 100 Inha-ro, Nam-Gu, Incheon, 22212, Republic of Korea

I. Introduction

THE recent development of a strapdown seeker with an Image Infra-Red (IIR) optical sensor, directly mounted on the missile body without any mechanical gimbal mechanism, is being researched to replace the gimballed seeker. However, there is a technical issue to be solved in order to utilize the strapdown seeker, since, in the case of the strapdown seeker, the LOS rate should be calculated or estimated to implement proportional navigation(PN)-type guidance laws. However, compared to the exact LOS rate, the computed LOS rate can be interpreted as a combination of the exact LOS rate term and an additional feedback term (i.e., the parasitic loop) caused by the mismatch of the measurements. This additional feedback loop eventually makes a guidance system unstable, and this phenomenon is called the parasitic effect of the strapdown seeker.

So far, very few previous works dealing with the above technical issue in the strapdown seeker have been reported in the public domain, despite its importance and urgency. Earlier studies on the strapdown seeker can be classified into two directions. First, some researchers have been putting their effort to investigate effects of the scale factor errors on a terminal homing guidance loop [1–4]. With this approach, the stability regions of the parasite loop, involving the strapdown homing seeker, were analyzed in several studies [5–8]. As the second research direction, some efforts have also been made to devise new homing guidance laws, corresponding terminal homing guidance loops[9–11], and guidance filters for the strapdown seeker[12–14].

As we can see above, the previous studies on the stability analysis mainly focused on the parasite effect caused by the scale factor errors. In the case of an IIR-type strapdown seeker, a time delay due to an IR image processing in order to discriminate and track the target on the image plane is an intrinsic property. Also, the differentiator (i.e., filter) to

*Research fellow, School of Aerospace, Transport and Manufacturing ; hong.ju.hyeon11@gmail.com

†Senior Researcher, Lumir Inc. ; radoba@naver.com

‡Assistant Professor, Department of Aerospace Engineering; chlee@fdcl.kaist.ac.kr

§Professor, Department of Aerospace Engineering; ckryoo@inha.ac.kr(Corresponding author)

generate the look angle rate can introduce a further time delay. If these time delays are involved, the homing loop with the strapdown seeker becomes unstable, even if the stability criteria of the scale factor errors are met. Therefore, the consideration of the parasitic effect caused by the time delays due to the IR image processing and the filtering is also crucial for designing the homing loop for the strapdown seeker. However, in the previous studies, this issue was not addressed well despite its importance.

Also, the previous studies on guidance laws and corresponding homing loop designs have not provided a direct solution to the parasite effect due to neither the scale factor errors nor the time delays i.e. a consideration of a field-of-view (FOV) effect only [10] or designing of pursuit-type guidance law [9]. Although the implementation of this guidance law could be free from the parasite effect, there is a price to pay in this approach. It is well-known that pursuit-type guidance laws are generally less effective than PN-type guidance laws in terms of the guidance performance due to the nature of pursuit guidance characteristic: less predictability when intercepting a target [15]. Therefore, instead of using pursuit-type guidance laws, if we can design a homing loop that is based on PN-type guidance laws (to guarantee the guidance performance) and that can mitigate the parasitic effect mainly due to the time delays (to ensure the stability), it will be beneficial for applications of the strapdown seeker.

In this context, this paper aims to investigate the parasitic effect due to the time delays of the IR image processing and the filtering, in order to broaden our understanding. Based on this analysis, a new homing loop that compensates for the parasitic effect induced by the time delays is proposed by utilizing the model matching method in conjunction with a modified PN-type guidance algorithm which is a PIDN (Proportional-Integral-Derivative Navigation) guidance law. To this end, in this paper, we first derive full nonlinear equations for LOS rates that are given by the equations of the look angle rates, body attitude angles, and body attitude angle rates. Operating under the assumption that the missile is well-stabilized in the roll channel, LOS rates in the pitch and yaw channel can be decoupled and simplified with the sum of the look angle rate and the body attitude angle rate in each channel. Therefore, based on the equations of the simplified LOS rates, we propose a design approach for a terminal homing loop of a missile with a three-axis rate gyro and a strapdown seeker. In the proposed approach, we purposely place a seeker-time-delay model and a filter for obtaining the look angle rate in the feedback signal loop of the body angular rate to mitigate the parasite effect, based on the concept of the model matching technique. Moreover, by introducing the PIDN law (which is motivated by the concept of PID control) for the homing guidance loop, the terminal homing loop can secure the stability margins even in the presence of the time delay errors after performing the model matching technique. In the proposed approach, we can directly analyze the stability and the dynamic characteristics of the homing loop in a straightforward manner. As an illustrative example, a design process is introduced for a stationary or slowly moving target, and the performance of the proposed homing loop is validated through nonlinear 6-DOF simulations.

The present paper is organized as follows: Section 2 presents a theoretical analysis of the LOS rates from the viewpoint of the coupling of the body attitude angles and the look angle rates. In Section 3, the parasitic effect due to the

time delays is investigated, and the new homing loop configuration is suggested, including the model matching and the PIDN guidance law to overcome instability as a result of the parasitic effect due to the time delays. Section 4 is devoted to a design example for a short-range tactical missile. Also, the stability of the proposed homing loop is analyzed and discussed. In addition, the performance of the proposed approach is verified via full nonlinear 6-DOF simulations, including Monte-Carlo analysis, according to various target ranges and time delays. Conclusions are found in Section 5.

II. Three Dimensional Geometric Interpretation of the LOS Rates

In this section, the relationship among the LOS rates, the look angles, and the body attitude rates is derived in the three-dimensional space, which will be used for the analysis in the next chapters. For the analysis purpose, we first make assumptions, which are used in this analysis, as follows:

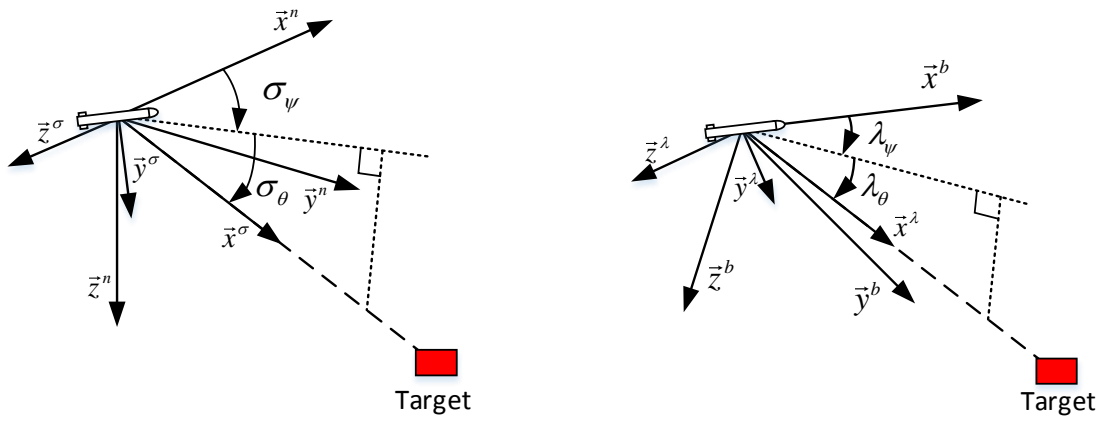
- The pitch and yaw channels can be decoupled since an autopilot for the roll channel is usually designed to be fast enough.
- The angle-of-attack remains a small value during the homing phase since the acceleration command (which is proportional to the angle-of-attack) gradually decreases during the homing phase under PN-type guidance laws.
- The look angle and LOS angle are considered as small values since the target remains within a narrow FOV of the strapdown seeker by a well-designed target tracking system.

Note that these assumptions are based on the literature [2, 16–21] and widely used for the analysis purpose in order to grasp general insights into the analysis by reducing the complexity.

In this study, we define the n -frame with x_n , y_n , and z_n axes of the reference coordinate system, which is used to define the body attitude angles. The fixed body coordinate system is also defined as the b -frame, where x_b , y_b , and z_b axes are respectively aligned with the roll, pitch, and yaw axes of the missile. The coordinate transformation matrix from the n -frame to the b -frame is defined by three consecutive 3-2-1 single rotations of the Euler angles as follows:

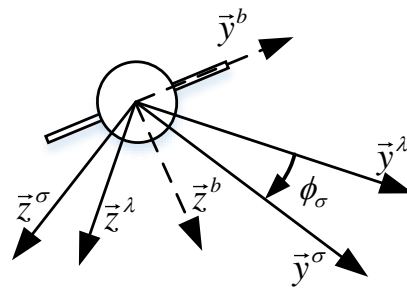
$$\begin{aligned}
 C_n^b &= R_1(\phi)R_2(\theta)R_3(\psi) \\
 &= \begin{bmatrix} 1 & 0 & 0 \\ 0 & c\phi & s\phi \\ 0 & -s\phi & c\phi \end{bmatrix} \begin{bmatrix} c\theta & 0 & -s\theta \\ 0 & 1 & 0 \\ s\theta & 0 & c\theta \end{bmatrix} \begin{bmatrix} c\psi & s\psi & 0 \\ -s\psi & c\psi & 0 \\ 0 & 0 & 1 \end{bmatrix} \\
 &= \begin{bmatrix} c\theta c\psi & c\theta s\psi & -s\theta \\ s\phi s\theta c\psi - c\phi s\psi & s\phi s\theta s\psi + c\phi c\psi & s\phi c\theta \\ c\phi s\theta c\psi + s\phi s\psi & c\phi s\theta s\psi - s\phi c\psi & c\phi c\theta \end{bmatrix}.
 \end{aligned} \tag{1}$$

where ψ , θ , and ϕ denote the yaw, pitch, and roll angles respectively. Additionally, the LOS coordinate system, which



(a) Definition of LOS angle.

(b) Definition of Look angle.



(c) Definition of roll angle in LOS frame.

Fig. 1 Definition of angles and coordinate systems.

is called the σ -frame with x_σ , y_σ , and z_σ axes is introduced. This coordinate system has its origin at the center of the mass of the missile. As shown in Figure 1, the x_σ -axis aligns the target along the LOS, and the target LOS angles are denoted by σ_ψ and σ_θ with respect to the n -frame. The coordinate transformation matrix from the n -frame to the σ -frame is given by

$$\begin{aligned}
C_n^\sigma &= R_2(\sigma_\theta)R_3(\sigma_\psi) = \begin{bmatrix} c\sigma_\theta & 0 & -s\sigma_\theta \\ 0 & 1 & 0 \\ s\sigma_\theta & 0 & c\sigma_\theta \end{bmatrix} \begin{bmatrix} c\sigma_\psi & s\sigma_\psi & 0 \\ -s\sigma_\psi & c\sigma_\psi & 0 \\ 0 & 0 & 1 \end{bmatrix} \\
&= \begin{bmatrix} c\sigma_\theta c\sigma_\psi & c\sigma_\theta s\sigma_\psi & -s\sigma_\theta \\ -s\sigma_\psi & c\sigma_\psi & 0 \\ s\sigma_\theta c\sigma_\psi & s\sigma_\theta s\sigma_\psi & c\sigma_\theta \end{bmatrix}.
\end{aligned} \tag{2}$$

The look-angle coordinate system, which is called the λ -frame with x_λ , y_λ , and z_λ axes, is also defined for convenience. The x_λ -axis directs the target and the target look angles are defined by λ_ψ and λ_θ with respect to the b -frame, as shown in Figure 2. The coordinate transformation matrix from the b -frame to the λ -frame is given by

$$C_b^\lambda = R_2(\lambda_\theta)R_3(\lambda_\psi) = \begin{bmatrix} c\lambda_\theta c\lambda_\psi & c\lambda_\theta s\lambda_\psi & -s\lambda_\theta \\ -s\lambda_\psi & c\lambda_\psi & 0 \\ s\lambda_\theta c\lambda_\psi & s\lambda_\theta s\lambda_\psi & c\lambda_\theta \end{bmatrix}. \tag{3}$$

Note that the x_σ -axis of the σ -frame is coincident with the x_λ -axis of the λ -frame. Hence, the σ -frame can be transformed from the λ -frame by rotating ϕ_σ along the x_λ -axis. Accordingly, the coordinate transformation matrix from the λ -frame to the σ -frame is defined by

$$C_\lambda^\sigma = R_1(\phi_\sigma) = \begin{bmatrix} 1 & 0 & 0 \\ 0 & c\phi_\sigma & s\phi_\sigma \\ 0 & -s\phi_\sigma & c\phi_\sigma \end{bmatrix}. \tag{4}$$

On the other hand, a consecutive coordinate transformation rule assures

$$C_\lambda^\sigma(\phi_\sigma) = C_n^\sigma(\sigma_\theta, \sigma_\psi)C_b^n(\phi, \theta, \psi)C_\lambda^b(\lambda_\theta, \lambda_\psi). \tag{5}$$

or

$$C_{\sigma}^n(\sigma_{\theta}, \sigma_{\psi})C_{\lambda}^{\sigma}(\phi_{\sigma}) = C_b^n(\phi, \theta, \psi)C_{\lambda}^b(\lambda_{\theta}, \lambda_{\psi}). \quad (6)$$

From Eq. (6), we have

$$\phi_{\sigma} = -\tan^{-1} \frac{c_{32}}{c_{33}}. \quad (7)$$

and

$$\sigma_{\psi} = \tan^{-1} \frac{c_{21}}{c_{11}}, \quad \sigma_{\theta} = -\tan^{-1} \frac{c_{31}}{\sqrt{c_{11}^2 + c_{21}^2}}. \quad (8)$$

where

$$\begin{aligned} c_{11} &= c\theta c\psi c\lambda_{\theta} c\lambda_{\psi} + c\lambda_{\theta} s\lambda_{\psi} (s\phi s\theta c\psi - c\phi s\psi) + s\lambda_{\theta} (c\phi s\theta c\psi + s\phi s\psi) \\ c_{21} &= c\theta s\psi c\lambda_{\theta} c\lambda_{\psi} + c\lambda_{\theta} s\lambda_{\psi} (s\phi s\theta s\psi + c\phi c\psi) + s\lambda_{\theta} (c\phi s\theta s\psi - s\phi c\psi) \\ c_{31} &= -s\theta c\lambda_{\theta} c\lambda_{\psi} + s\phi c\theta c\lambda_{\theta} s\lambda_{\psi} + c\phi c\theta s\lambda_{\theta} \\ c_{32} &= s\theta s\lambda_{\psi} + s\phi c\theta c\lambda_{\psi} \\ c_{33} &= s\theta s\lambda_{\theta} c\lambda_{\psi} - s\lambda_{\theta} s\lambda_{\psi} s\phi c\theta + c\phi c\theta c\lambda_{\theta} \end{aligned} \quad (9)$$

Note that these parameters are given by the functions of the Euler angles and look angles, which can be measured by an onboard INS and a strapdown seeker. Next, let $\vec{\omega}_{n\lambda}^{\lambda}$ denote the look angle rate vector, or the angular rate vector of the λ -frame, with respect to the n -frame, which is defined in the λ -frame. Then,

$$\vec{\omega}_{n\lambda}^{\lambda} = C_b^{\lambda} \vec{\omega}_{nb}^b + \vec{\omega}_{b\lambda}^{\lambda}. \quad (10)$$

where $\vec{\omega}_{nb}^b$ denotes the body angular rate vector with respect to the n -frame, represented in the b -frame, and $\vec{\omega}_{b\lambda}^{\lambda}$ denotes the look angle rate vector with respect to the b -frame, represented in the λ -frame. Let the roll, pitch, and yaw rates of the missile be defined as p , q , and r , which are typically measured by the rate gyro, then

$$\vec{\omega}_{nb}^b = \begin{bmatrix} p & q & r \end{bmatrix}^T. \quad (11)$$

And let us define the time derivatives of λ_{ψ} and λ_{θ} as $\dot{\lambda}_{\psi}$ and $\dot{\lambda}_{\theta}$, which are obtained by the filter, then

$$\vec{\omega}_{b\lambda}^{\lambda} = C_b^{\lambda} \begin{bmatrix} 0 & 0 & \dot{\lambda}_{\psi} \end{bmatrix}^T + R_2(\lambda_{\theta}) \begin{bmatrix} 0 & \dot{\lambda}_{\theta} & 0 \end{bmatrix}^T. \quad (12)$$

Substituting Eqs. (3), (11) and (12) into Eq. (10) gives

$$\vec{\omega}_{n\lambda}^\lambda \triangleq \begin{bmatrix} p_\lambda & q_\lambda & r_\lambda \end{bmatrix}^T = \begin{bmatrix} p \cos \lambda_\theta \cos \lambda_\psi + q \cos \lambda_\theta \sin \lambda_\psi - (r + \dot{\lambda}_\psi) \sin \lambda_\theta \\ -p \sin \lambda_\psi + q \cos \lambda_\psi + \dot{\lambda}_\theta \\ p \sin \lambda_\theta \cos \lambda_\psi + q \sin \lambda_\theta \sin \lambda_\psi + (r + \dot{\lambda}_\psi) \cos \lambda_\theta \end{bmatrix}. \quad (13)$$

Let $\vec{\omega}_{n\sigma}^\sigma$ denote the LOS rate vector with respect to the n -frame, which is defined in the σ -frame, then,

$$\vec{\omega}_{n\sigma}^\sigma = C_\lambda^\sigma \vec{\omega}_{n\lambda}^\lambda + \vec{\omega}_{\lambda\sigma}^\sigma. \quad (14)$$

where $\vec{\omega}_{n\lambda}^\lambda$ denotes the look angle rate vector with respect to the n -frame, represented in the λ -frame, and $\vec{\omega}_{\lambda\sigma}^\sigma$ denotes the LOS rate vector with respect to the λ -frame, represented in the σ -frame. Let us denote the time derivatives of σ_ψ and σ_θ as $\dot{\sigma}_\psi$ and $\dot{\sigma}_\theta$, then

$$\vec{\omega}_{n\sigma}^\sigma = C_n^\sigma \begin{bmatrix} 0 & 0 & \dot{\sigma}_\psi \end{bmatrix}^T + R_y(\sigma_\theta) \begin{bmatrix} 0 & \dot{\sigma}_\theta & 0 \end{bmatrix}^T \quad (15)$$

Recalling that the x_σ -axis and the x_λ -axis are in the same direction, the σ -frame is obtained by rotating ϕ_σ along with the x_λ -axis of the λ -frame. It means

$$\vec{\omega}_{\lambda\sigma}^\sigma = \begin{bmatrix} \dot{\phi}_\sigma & 0 & 0 \end{bmatrix}^T. \quad (16)$$

Therefore, substituting Eqs. (4), (13), (15) and (16) into Eq. (14) yields

$$\dot{\phi}_\sigma = -p_\lambda + \tan \sigma_\theta (q_\lambda \sin \phi_\sigma - r_\lambda \cos \phi_\sigma). \quad (17)$$

and

$$\begin{aligned} \dot{\sigma}_\theta &= q_\lambda \cos \phi_\sigma + r_\lambda \sin \phi_\sigma \\ \dot{\sigma}_\psi &= -\frac{q_\lambda \sin \phi_\sigma - r_\lambda \cos \phi_\sigma}{\cos \sigma_\theta}. \end{aligned} \quad (18)$$

where ϕ_σ , σ_θ , and σ_ψ are given by Eqs. (7) and (8) in terms of the Euler angles and the look angles. The LOS rates given in Eq. (18) can be used for PN-type guidance laws. From the aspect of implementation, $(\lambda_\psi, \lambda_\theta)$ are directly measured by the strapdown seeker, $(\dot{\lambda}_\psi, \dot{\lambda}_\theta)$ are estimated by the filter or differentiator, (ψ, θ, ϕ) and (p, q, r) are measured by the INS, and σ_θ is given by the geometric relationship between the missile and the target.

As mentioned above, if we assume that the target remains within a narrow FOV of the strapdown seeker of the missile during the engagement, the small angle approximation is possible. Under this approximation, both C_λ^σ and the

look angle can be approximated as follows, using both Eqs. (4) and (5) and, we have the following relationships as

$$\begin{aligned}
 \phi_\sigma &= -\phi \\
 \sigma_\theta &= \theta + \lambda_\theta \\
 \sigma_\psi &= \psi + \lambda_\psi.
 \end{aligned} \tag{19}$$

Also, under the small angle approximation of the look angles and LOS angles, we have

$$\begin{aligned}
 \dot{\sigma}_\theta &\approx q + \dot{\lambda}_\theta - \lambda_\psi p - (r + \dot{\lambda}_\psi)\phi \\
 \dot{\sigma}_\psi &\approx r + \dot{\lambda}_\psi + \lambda_\theta p + (q + \dot{\lambda}_\theta)\phi.
 \end{aligned} \tag{20}$$

We readily observe that Eq. (20) confirms that the LOS rates are in a form where the roll angle and roll rate are coupled with the elements of different channels. If the missile is stabilized adequately in the roll channel as mentioned before, we have the simplest form of LOS rates.

$$\begin{aligned}
 \dot{\sigma}_\theta &\approx q + \dot{\lambda}_\theta \\
 \dot{\sigma}_\psi &\approx r + \dot{\lambda}_\psi.
 \end{aligned} \tag{21}$$

Note that the LOS rate can be expressed by the function of the pitch rate, the yaw rate, and the look angles. Therefore, the minimum sensor requirements for computing the LOS rate given in Eq. (21) are the rate gyros to measure the pitch and the yaw rates and the strapdown seeker in order to measure the look angles. Additionally, the filter, or differentiator, to produce the look angle rates is still required. A roll rate gyro should be additionally equipped for roll stabilization of the missile. Therefore, under the approximation of small angles and roll stabilization, the three-axis rate gyros with the strapdown seeker is sufficient for computing the LOS rates, without the need for the INS.

III. Homing Loop Design for Compensating the Parasitic Effect

A. Investigation of Parasite Loop due to the Time Delays

In this section, we investigate the parasite effect or parasite loop due to the time delays in the homing guidance loop under the pure PN law. Applying the pure PN law, the guidance commands normal to the missile velocity in the pitch and yaw channels, denoted by a_z and a_y respectively, are given by

$$\begin{aligned}
 a_z &= NV_m \dot{\sigma}_\theta + g_z^n \\
 a_y &= NV_m \dot{\sigma}_\psi.
 \end{aligned} \tag{22}$$

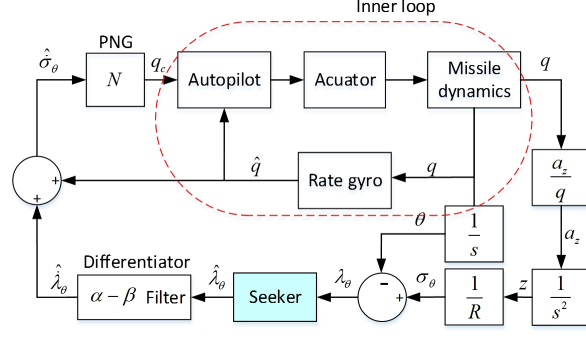


Fig. 2 The terminal homing loop in the pitch channel.

where N is the proportional navigation constant, V_m is the missile speed, and g is the gravitational acceleration for gravity compensation. If we neglect the angle-of-attack by the assumption as mentioned before, the acceleration commands can be converted to the pitch and yaw rate commands, which are denoted by q_c and r_c respectively. Therefore, the pitch and yaw rate commands can be expressed by substituting Eq. (21) into Eq. (22) as follows:

$$\begin{aligned} q_c &\approx N (\dot{\lambda}_\theta + q) + \frac{g_z^n}{V_m} \\ r_c &\approx N (\dot{\lambda}_\psi + r). \end{aligned} \quad (23)$$

Note that the pitch channel and the yaw channel can be decoupled, and the gravity compensation term in the pitch channel can be omitted for the analysis purpose because it does not affect the stability of the system. Accordingly, it can be regarded as both channels have the same structure. Thus, from now on we investigate the characteristics of the pitch channel only. The terminal homing loop in the pitch channel without the gravity compensation term is given as shown in Figure 2, and the terminal homing loop is based on the miss distance dynamics with the LOS angle reconstruction, which was presented in [22, 23]. In this figure, the measured look angle and the pitch rate are denoted by $\hat{\lambda}_\theta$ and \hat{q} respectively. The estimated look angle rate and the resulting LOS rate are represented by $\hat{\lambda}_\theta$ and $\hat{\sigma}_\theta$ respectively.

Since $\hat{\sigma}_\theta$ is given by Eq. (21), in order to implement Eq. (23), we need to know the pitch look angle rate $\dot{\lambda}_\theta$, which is usually estimated by a filter such as the $\alpha - \beta$ filter that works well for noisy measurements. The $\alpha - \beta$ filter to estimate the look angle rate at the k -th time step is given by [24, 25]

$$\begin{aligned} \hat{\lambda}_\theta(k) &= \hat{\lambda}_\theta(k-1) + T\hat{\lambda}_\theta(k-1) + \alpha \left[\lambda_\theta(k) - \hat{\lambda}_\theta(k-1) - T\hat{\lambda}_\theta(k-1) \right] \\ \hat{\lambda}_\theta(k) &= \hat{\lambda}_\theta(k-1) + \frac{\beta}{T} \left[\lambda_\theta(k) - \hat{\lambda}_\theta(k-1) - T\hat{\lambda}_\theta(k-1) \right]. \end{aligned} \quad (24)$$

where T is the sampling interval, and the filter gains (α and β) are given by the functions of the process and measurement

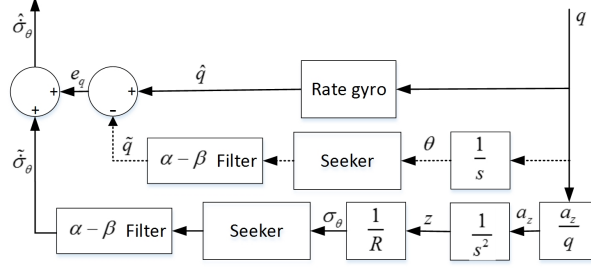


Fig. 3 The hidden parasite loop in the terminal homing loop.

noise covariances, which are denoted by σ_w and σ_n respectively

$$\alpha = 1 - \frac{\beta^2}{\Lambda^2}, \quad \beta = \frac{\Lambda}{4} \left(\Lambda + 4 - \sqrt{\Lambda^2 + 8\Lambda} \right), \quad \Lambda = \frac{T^2 \sigma_w}{\sigma_n}. \quad (25)$$

Here, the lower part of the homing loop of Figure 2 can be equivalently restructured as shown in Figure 3, for the purpose of investigating the signal flow. From Figure 3, it turns out that the mechanism of producing $\hat{\sigma}_\theta$ is carried out by canceling the pitch rate \tilde{q} which is implicitly embedded in the look angle rate by the pitch rate \hat{q} which is measured by the rate gyroscope. However, the signal flows for both \tilde{q} and \hat{q} have different dynamics because of the time delays, so that the error source e_q , which is the difference between the seeker's attitude rate \tilde{q} and the gyroscope's attitude rate \hat{q} , cannot be perfectly nullified. Accordingly, the signal flow for \tilde{q} forms a parasitic loop, which is hidden in the homing loop, for the strapdown seeker, and the positive feedback of e_q makes the system unstable if a PN-type guidance law is applied to the system. Moreover, since the $\alpha - \beta$ filter of the differentiator usually acts as a high pass filter, it can make this instability worse by allowing to pass and magnify a high-frequency signal. This is the parasitic effect due to the time delays in the strapdown seeker.

B. The proposed homing loop structure

In this section, we introduce the proposed homing loop structure in order to compensate for the parasite effect as mentioned above. Since the parasite loop is mainly caused by a mismatch of the two signal flows \tilde{q} and \hat{q} due to the time delays of the IR image processing and the filtering, we first minimize the mismatch by utilizing the model matching technique [25]. From a practical point of view, the processing time for obtaining the IR image and determining the look angle can be modelled as pure delay as

$$G_{SD}(s) = e^{-T_{SD}s}. \quad (26)$$

or in the digital domain

$$H_{SD}(z) = z^{-T_{SD}/T}. \quad (27)$$

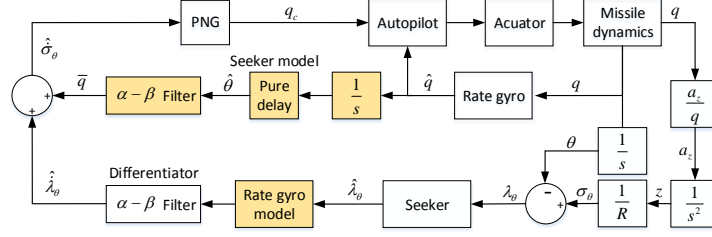


Fig. 4 Model matching for compensation of the parasitic loop.

where T_{SD} and T represent the time delay for the strapdown seeker and the fixed time at each step of the simulation. Additionally, Pade approximation analysis is used to transform the exponential function in Eq. (26) into a rational linear transfer function[26]. And then, in order to compensate for the parasitic loop, we put the pure delay (the strapdown seeker's processing time) and the $\alpha - \beta$ filter in the signal flow of \hat{q} as shown in Figure 4, by utilizing the model matching technique. By doing so, the error e_q in Figure 3 can be nullified, if both the dynamics of the rate gyro is neglected and the seeker delay is exactly known.

Although the model matching technique can help mitigate the parasite loop due to the mismatch of the two signals, it cannot completely eliminate the parasite loop because the seeker delay is not precisely known in practice. Additionally, even though the parasite loop is perfectly eliminated by the model matching technique, the homing loop may become unstable due to the modeling errors in the aerodynamic coefficients, actuator dynamics, and gyroscope dynamics. This is because the modeling errors typically reduce the phase margin, and decreasing of the phase margin results in decreasing of the delay margin. Therefore, these facts imply that an appropriate guidance algorithm is also required to ensure the homing loop stability even in the presence of the time delay errors after applying the model matching technique as well as the modeling errors.

From Figure 4, we can readily notice that the PN guidance law can act as the proportional (P) control to nullify $\hat{\sigma}_\theta$ in the homing loop, where the proportional navigation constant N can be regarded as the P-gain. This fact suggests the possibility of modified PN-type guidance laws that can improve the homing loop stability against the time delay errors and the modeling errors. To be more specific, in the field of control theory, it is well-known that the concept of derivative (D) or integral (I) control is an effective way to compensate for a time delay error and an external disturbance (or modeling error). Based on this aspect, we can exploit the benefit of D or I control concept in the homing loop design by modifying the PN guidance law Eq. (22) as follows

$$a_z = K_P V_m \dot{\sigma}_\theta + K_D V_m \frac{d}{dt} \dot{\sigma}_\theta + K_I V_m \int \dot{\sigma}_\theta dt + g_z^n. \quad (28)$$

In this study, we call it as PIDN (Proportional-Integral-Derivative Navigation) law. The parameter K_P is the same as

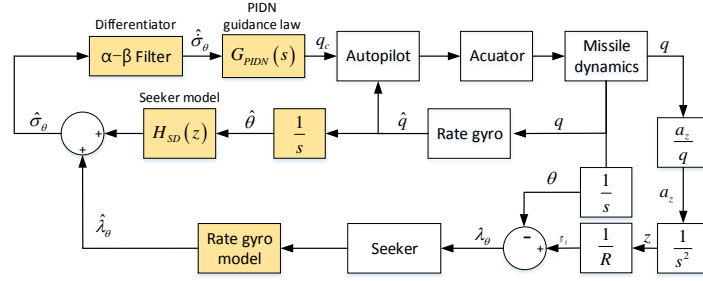


Fig. 5 The proposed structure of the homing loop.

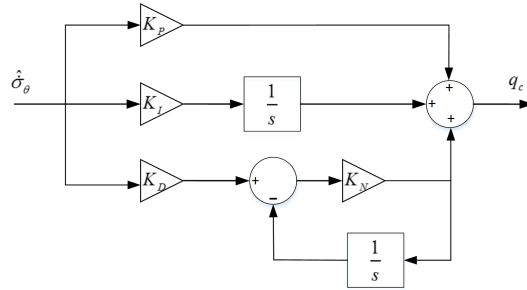


Fig. 6 The structure of the PIDN law for implementation in the homing loop.

the proportional navigation constant N . The other parameters K_D and K_I are considered as the derivative navigation constant and the integral navigation constant, respectively. Accordingly, if we reconstruct the homing loop using the PIDN law without the gravity compensation term, the proposed homing loop becomes a diagram as shown in Figure 5, where the colored blocks are design elements. Through appropriate selections of K_P , K_D and K_I in the PIDN law, we can ensure the gain and phase margin, but also the delay margin in order to prevent the instability of the system due to the time delay of the seeker. Especially, the structure of the PIDN law for implementation in the homing loop is depicted in Figure 6, where the parameter K_N represents the gain for the embedded differentiator.

The delay margin, which has the dimension of time, is defined by dividing the phase margin by the gain crossover frequency. According to the linear control theory, there are the following two ways of increasing the delay margin of the system: making the gain crossover frequency small or making the phase margin large. A smaller gain crossover frequency tends to make the bandwidth of the system narrow, and a larger phase margin leads the system to dull. Hence, a balanced selection of both parameters is essential to guarantee the stability and performance of the system. The delay margin as the design criteria should be satisfied more than the system delay to secure the system's stability for the entire flight region.

Table 1 The derivatives of the aerodynamic coefficients.

Mach no.	$Z_\alpha(1/s)$	$M_\alpha(1/s^2)$	$M_q(1/s)$	$Z_\delta(1/s)$	$M_\delta(1/s^2)$
0.3	-1.94	-533.20	-0.61	-0.49	224.91
0.5	-3.34	-1456.84	-1.11	-0.86	691.81
0.7	-4.63	-2980.71	-1.72	-1.26	1505.32

IV. Illustrative Design Examples

A. Homing loop design with missile model and autopilot

We consider a short-range tactical missile with a strapdown seeker and a three-axis rate gyro for numerical simulations to verify the performance of the proposed homing loop as discussed in the previous section. The missile is aerodynamically controlled with a maximum range of 2,500, intended to attack ground vehicles or bunkers as major targets. The sampling rate of the homing loop is assumed to be 10 ms. Detailed specifications of the missile are omitted except for the parameters related to the linearized model for the homing loop design, as shown in Table 1.

In Figure 2, the outer loop (i.e., the guidance law) produces the pitch rate guidance command to intercept the target, and the inner loop (i.e., the autopilot) produces fin deflection angles that satisfy the pitch rate command. The transfer function from the fin deflection angle to the pitch rate is given by

$$\frac{q(s)}{\delta_p(s)} = \frac{M_\delta s + (M_\alpha Z_\delta - Z_\alpha M_\delta)}{s^2 - (Z_\alpha + M_q)s + (Z_\alpha M_q - M_\alpha)}. \quad (29)$$

Usually, the proportional controller is adequate for the autopilot. For the designing purpose of the inner loop, we approximated that the actuator's transient response can be ignored since the actuator response is much faster than the inner loop response. Under this approximation, the transfer function of the pitch rate to the pitch rate command is given by

$$\frac{q(s)}{q_c(s)} = \frac{K_{qt} K_q [M_\delta s + (M_\alpha Z_\delta - Z_\alpha M_\delta)]}{s^2 + 2\zeta_q \omega_q s + \omega_q^2}. \quad (30)$$

where

$$\begin{aligned} 2\zeta_q \omega_q &= K_q M_\delta - Z_\alpha - M_q \\ \omega_q^2 &= Z_\alpha M_q - M_\alpha + K_q (M_\alpha Z_\delta - Z_\alpha M_\delta). \end{aligned} \quad (31)$$

where Z_α , M_α , M_q , Z_δ , M_δ are the dimensional aerodynamic and control derivatives shown in Table 1. ζ_q and ω_q , respectively, denote the damping coefficient and the natural frequency, which are the design objectives of the controller to be satisfied by proper selection of the controller gains of K_q and K_{qt} , as included in Table 2; we can see the autopilot has enough gain and phase stability margins.

Figure 7 shows the structure of autopilot, which is utilized to tune the autopilot gain K_q and K_{qt} , and G_a is the

Table 2 The gain sets of inner-loop autopilot.

Mach no.	σ_q	$\omega_q(\text{rad/s})$	K_q	K_{qt}	Gain margin(dB)	Phase margin(deg)
0.3	0.5	24.5	9.78e-2	8.84	18.44	75.17
0.5	0.45	40.3	4.60e-2	9.92	14.89	65.59
0.7	0.45	57.6	3.02e-2	10.22	11.24	51.40

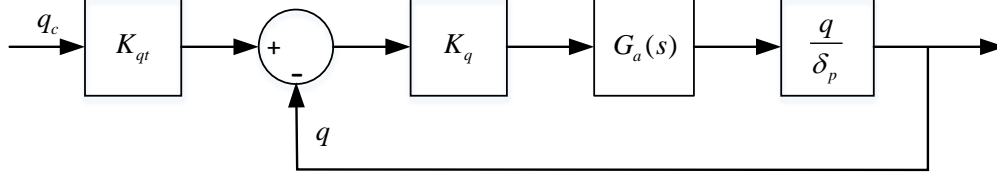


Fig. 7 The structure of the autopilot for implementation in the homing loop.

second order actuator model as given by

$$G_a(s) = \frac{\omega_{n_a}^2}{s^2 + 2\zeta_a\omega_{n_a}s + \omega_{n_a}^2} \quad (32)$$

where the natural frequency ω_{n_a} and the damping coefficient ζ_a of the second order actuator model are determined as follows

$$\omega_{n_a} = 25Hz, \zeta_a = 0.6 \quad (33)$$

The lateral acceleration in the time domain is given by

$$a_z(t) = \frac{V_m}{g_z^n}(\dot{\alpha}(t) - q(t)) + \frac{\bar{x}}{g_z^n}\dot{q}(t) \quad (34)$$

where \bar{x} is the distance between the center of mass and the accelerometer.

From Eq.(34), the resultant transfer function of the lateral acceleration to the fin deflection angle in the pitch channel is given by

$$\frac{a_z(s)}{\delta_p(s)} = \frac{(V_m Z_\delta + \bar{x} M_\delta) s^2 - [V_m Z_\delta M_q + \bar{x}(M_\delta Z_\alpha - M_\alpha Z_\delta)] s + V_m(M_\delta Z_\alpha - M_\alpha Z_\delta)}{g[s^2 - (Z_\alpha + M_q)s + (Z_\alpha M_q - M_\alpha)]}. \quad (35)$$

Thus, the transfer function of the lateral acceleration to the pitch rate is given by

$$\begin{aligned} \frac{a_z(s)}{q(s)} &= \frac{a_z(s)}{\delta_p(s)} \frac{\delta_p(s)}{q(s)} \\ &= \frac{(V_m Z_\delta + R M_\delta) s^2 - [V_m Z_\delta M_q + R(M_\delta Z_\alpha - M_\alpha Z_\delta)] s + V_m(M_\delta Z_\alpha - M_\alpha Z_\delta)}{g[M_\delta s + (M_\alpha Z_\delta - Z_\alpha M_\delta)]}. \end{aligned} \quad (36)$$

Furthermore, the gyroscope model and $\alpha - \beta$ filter model, which are utilized in the design example, are given by

$$G_{gyro}(s) = \frac{\omega_{n_g}^2}{s^2 + 2\zeta_g \omega_{n_g} s + \omega_{n_g}^2} \quad (37)$$

$$G_{filter}(z) = \frac{(\beta/\Delta T) z(z-1)}{z^2 - (2-\alpha-\beta)z + 1-\alpha} \quad (38)$$

where the natural frequency ω_{n_g} and damping coefficient ζ_g of the second order gyroscope model are defined in Eq.(39), and the filter's coefficients α and β and sampling time of the guidance loop ΔT are defined in Eq.(40) respectively.

$$\omega_{n_g} = 100Hz, \zeta_g = 0.707 \quad (39)$$

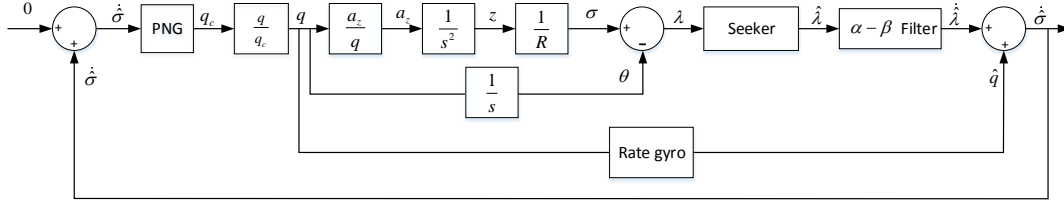
$$\alpha = 0.9944, \beta = 1.7123, \Delta T = 0.02s \quad (40)$$

B. Linear stability analysis and discussion

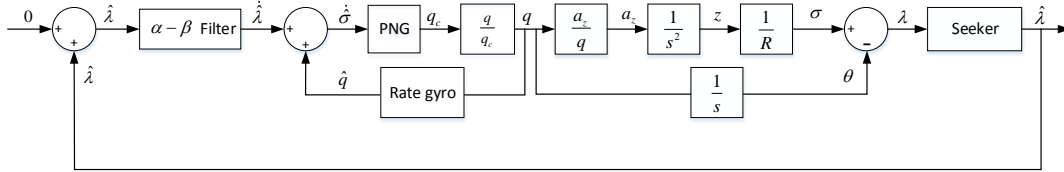
In order to analyze the linear stability, the homing loop of Figure 2 can be converted to the loop in Figure 8. Since the homing loop acts the regulator, which the LOS rate makes zero, the gain margin and phase margin can be analyzed by using the loop as shown in Figure 8a. In addition, since the time delay of the homing loop is mainly generated at the seeker output, which calculates the look angle, we analyze the delay margin with the loop as shown in Figure 8b. Similarly, the homing loops of Figure 4 and 5 can be converted and analyzed in the same way.

1. The initial setup for the homing loop with PN gain

In case there is no time delay in the seeker as given in Figure 2, the gain and phase margins of the entire PN homing loop with $N = 3$ are 17.4 dB and 88.5° respectively, while the delay margin is just 1 ms at the $M=0.6$ and $R=500$ m. If a non-zero seeker delay greater than the delay margin is involved, the homing loop becomes unstable. Very small N , less than 0.1, can barely stabilize the homing loop, but a huge guidance error is produced.



(a) Linear loop for the gain and phase margin.



(b) Linear loop for the delay margin.

Fig. 8 Linear homing loops for stability analysis.

2. The model matching homing loop with PN gain

In Figure 4, an integrator, a delay component, and the $\alpha - \beta$ filter purposely places on the rate gyro signal flow to match with the seeker signal, and this structure can stabilize the homing loop. Even in the case where the homing loop includes a seeker delay of 60 ms, the 24.6 dB gain margin and 84.8° phase margin is achieved at the $M=0.6$ and $R=500$ m. Although the gain and phase margins are sufficient, the delay margin is 1.9 ms and still small. This implies that the model matching method effectively solves the problem due to the parasitic loop if the system models including seeker delay are precisely known. However, if the seeker delay or other model components have some modeling errors, the model matching method cannot improve the stability. For example, if the true time delay of the seeker is 80 ms, while the seeker delay is modeled with a 60 ms delay, the homing loop as given in Figure 4 is unstable, since a 20 ms delay difference between the true and model seeker is greater than a 1.9 ms delay margin. Even though we know precisely the delay of the seeker, the homing loop may become unstable due to the modeling errors in the aerodynamic coefficients, actuator dynamics, and gyroscope dynamics. The modeling errors typically make the phase margin small, and this reduced amount of the phase margin can be converted to the reduced amount of the delay margin, which is given by

$$\text{The reduced delay margin} = \frac{\text{The reduced amount of the phase margin}}{\text{The gain cross-over frequency}}. \quad (41)$$

If the reduced delay margin is greater than the delay margin, the homing loop will become unstable. Suppose that the gain crossover frequency of the homing loop of Figure 4 is 50 rad/s and the reduced amount of the phase margin due to modeling error is 10° , then the amount of reduced delay margin is 3.5 ms. This is greater than the delay margin of 1.9 ms, and in this case, the homing loop becomes unstable.

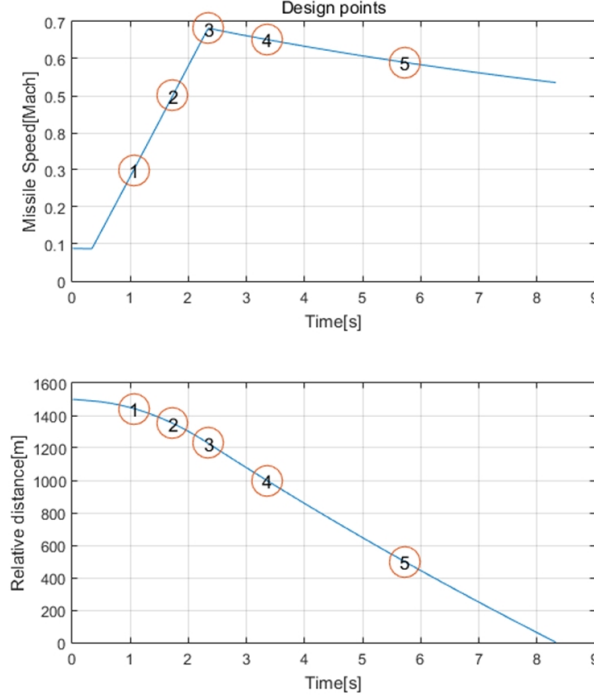


Fig. 9 Design point candidates for selecting gain set (Initial target range: 1,500 m).

3. The proposed homing loop with PIDN law

As discussed above, the seeker delay is one of the most crucial factors that make the homing loop with strapdown seeker unstable by association with the parasitic effect. Hence, the design strategy to ensure the delay margin of the system should be considered for the homing loop with the strapdown seeker. The proportional gain N , the navigation constant of the PN law, is not enough to ensure the delay margin of the homing loop, so we use the PIDN law instead of the PN law, as shown in Figure 5.

First, we have to select appropriate parameters for the PIDN law G_{PID} in the homing loop. The transfer function of the homing loop varies according to the remaining range R as well as the missile speed V_m , as given in Eq.(36). In order to guarantee the best performance, the gain scheduling according to V_m and R is required. However, because, R is not measurable by the current missile sensor systems—comprising a strapdown seeker and a three-axis rate gyro—, the gain scheduling is not available. Instead of gain scheduling, we apply only one gain set for the entire flight conditions and just check the stability of the homing loop at off-design points. After elaborated simulations, we choose the design point of 5 in Figure 9 to select the gain set, i.e., $M = 0.59$ and $R = 500$ m, where the initial target range is 1,500 m, the most frequently engaged target.

Table 3 shows the stability margins of the homing loop for Figure 5, for each design point and the delay margins, as well as the ensured gain and phase margins. Table 4 shows the results of the stability analysis at the off-design points under the application of a single gain set at design point 5 in Figure 9.

Table 3 The gain sets of the PIDN law.

Design point	Speed (M)	Rel. dist. (m)	K_P	K_I	K_D	K_N	SettlingTime (s)	GM (dB)	PM (deg)	DM (s)
1	0.3	1442	11.21	0.03	-18.5	0.61	14.99	31.34	63.27	0.117
2	0.5	1351	6.78	0.03	-5.59	1.21	7.64	25.75	62.45	0.020
3	0.68	1229	2.70	0.01	-2.54	1.06	9.08	27.49	63.92	0.037
4	0.65	1000	2.38	0.01	-2.13	1.12	8.98	27.58	65.02	0.409
5	0.59	500	2.00	0.01	-1.51	1.33	6.84	24.76	61.57	0.454

The gain margin is minimal with a value of 1.67 dB at point 2 with a +40 ms delay error. The minimum delay margin with a value of about 66 ms is achieved at point 5 with a +20ms delay error, but there is still enough room for compensating for the time delay errors.

C. Performance verification via nonlinear 6-DOF simulations

A nonlinear 6-DOF simulation was carried out to verify the guidance performance of the proposed homing loop based on the PIDN law. Simulation conditions are shown in Table 5. The following three different time delay errors are considered: no time delay, 20 ms faster than the actual delay time, and 20 ms slower than the actual delay time.

Nonlinear simulation results for the initial target ranges of 500 m and 1,000 m, under no disturbances including zero time delay error, are shown in Figure 10 and Figure 11 respectively, where the miss distances are all less than one meter. Slight altitude losses in the very initial flight phase due to tip-off are observed, but here we are not concerned about a ground crash. Figure 12 shows the simulation results for the initial target range of 1,500 m under the disturbances of a 10 m/s crosswind with counter direction to target movement. The miss distances, in this case, is slightly increased but less than 1.5 m. Due to the crosswind, the trajectory on the horizontal plane shows a far more curved path and the target is within the FOV of 12° during the entire flight. Heavy crosswind may cause the strapdown seeker to lose target lock-on.

Now, we investigate the performance of the proposed homing loop under various uncertainties via a Monte-Carlo simulation. Uncertainties in the aerodynamic coefficients and seeker measurement noise and winds are defined in Table 6 for a Monte-Carlo simulation with 250 runs and a confidence level of 95% or higher [27]. The target is initially 1,500 m away from the missile launch point and moves with the constant velocity of (5 m/s, 5 m/s). We observe from Table 7 that the proposed homing loop shows good performance with a resultant mean miss distance of about 2 m and Circular Error Probable (CEP) within 0.6 m.

Table 4 The stability margins at off-design points.

Time delay error	Stability margins	1	2	3	4	5
-40 ms	G. M.(dB)	7.40	9.44	4.78	6.27	9.33
	P. M(deg)	81.67	79.75	72.04	70.26	60.99
	D. M.(s)	1.351	0.539	0.357	0.375	0.413
-20 ms	G. M.(dB)	14.86	13.26	4.33	5.68	8.53
	P. M(deg)	81.67	79.78	72.19	70.44	61.28
	D. M.(s)	1.388	0.568	0.381	0.399	0.434
0 ms	G. M.(dB)	46.32	36.36	30.12	29.10	24.76
	P. M(deg)	81.66	79.80	72.35	70.62	61.57
	D. M.(s)	1.426	0.597	0.406	0.423	0.454
+20 ms	G. M.(dB)	10.15	6.43	8.03	7.73	7.10
	G.M.(dB)	81.66	79.82	72.50	70.80	61.86
	D. M.(s)	1.465	0.075	0.429	0.447	0.066
+40 ms	G. M.(Bd)	3.39	1.67	3.77	3.44	2.74
	P. M(deg)	81.66	79.84	72.65	70.98	62.13
	D. M.(s)	1.504	0.086	0.453	0.470	0.090

Table 5 Initial conditions for 6-DOF simulation.

Parameters	Initial value
Initial missile position	(0 m, 0 m, 0 m)
Initial target position	(1500 m, 0 m, 0 m)
Initial velocity of target	(10 m/s, 10 m/s, 0 m/s)
Real seeker delay time	60 ms
Loop sampling time	10 ms

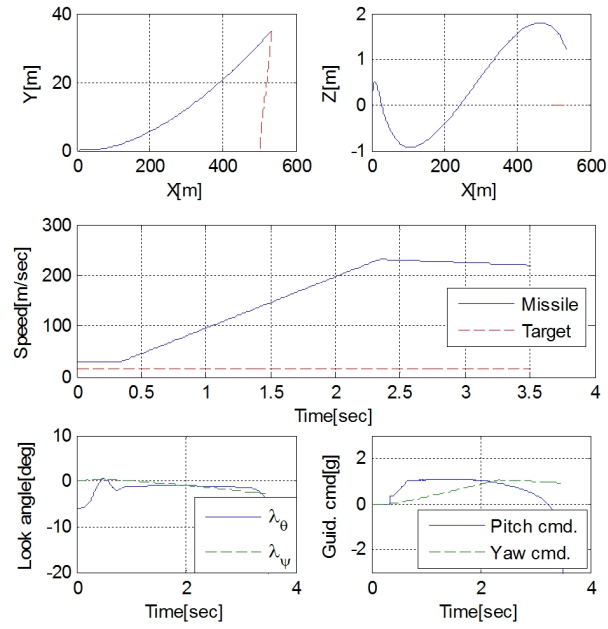


Fig. 10 Simulation results for the initial target range of 500m(No disturbances).

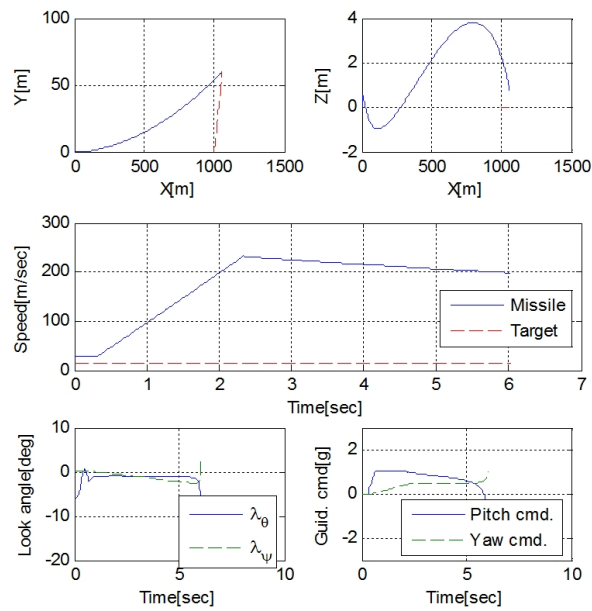


Fig. 11 Simulation results for the initial range of 1000m(No disturbances).

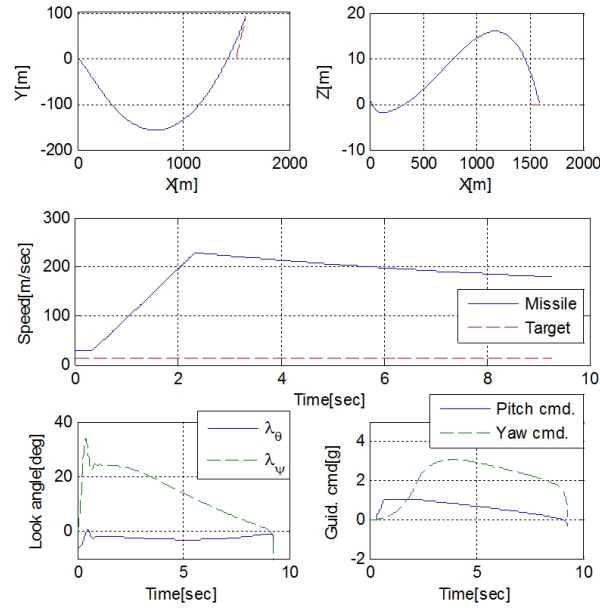


Fig. 12 Simulation results for the initial range of 1,500m under crosswind.

Table 6 Uncertainties for the Monte Carlo Simulation.

Error elements	Uncertainty	Probability distribution	Random number types	STD (1σ), range
Environmental error	Wind direction (deg)	Uniform	Run-wise	0–180
	Wind speed (m/s)	Normal	Run-wise	3
Missile model error	Force-related aerodynamic coefficient (%)	Normal	Run-wise	2
	Moment-related aerodynamic coefficient (%)	Normal	Run-wise	1
Seeker errors	Look angle error (deg)	Normal	Path-wise	0.1

Table 7 Monte Carlo Simulation Results.

Seeker time delay Error	CEP	Average miss distance(x,y)
-20ms	0.60m	0.16m, 1.87m
-40ms	0.17m	0.15m, 1.86m
20ms	0.26m	0.18m, 1.80m
40ms	0.41m	0.19m, 1.80m
0ms	0.47m	0.05m, 2.04m

V. Conclusions

In this paper, the parasite effect due to the time delay, which has been ignored despite its importance, was investigated. It was found that the time delay due to the infrared (IR) image processing and the filtering is a main reason of the parasite effect, and it was shown that the unstable home guidance loop can be stable by securing enough delay margin. In accordance with this manner, a homing guidance loop design approach that uses the model matching method in conjunction with a modified proportional navigation (PN) type guidance algorithm was proposed. The performance of the proposed approach was verified via nonlinear 6-DOF simulations, and the miss distances in relation to a moving target with or without wind disturbances are below 1 and 1.5 m, respectively. In addition, the Monte Carlo simulation was performed to verify the proposed homing loop under various uncertainties; the mean miss distance is 2 m, and the circular error probable (CEP) is below 0.6 m. Moreover, the physical dynamics and the stability of the proposed guidance law can be analyzed straightforwardly. Because the proposed approach is based on the structure of the well-known PN law and a conventional control system, the proposed approach can be applied to a real system without any difficulty.

Funding Sources

This paper is based upon work supported by the Agency for Defense Development of Korea under Contract Number UD160072BD.

References

- [1] Willman, W. W., "Effects of strapdown seeker scale-factor uncertainty on optimal guidance," *Journal of Guidance, Control, and Dynamics*, Vol. 11, No. 3, 1988, pp. 199–206. doi:10.2514/3.20294.
- [2] Mehra, R. K., and Ehrich, R. D., "Air-Tk-Air Missile Guidance For Strapdown Seekers," *The 23rd IEEE Conference on Decision and Control*, IEEE, Las Vegas, 1984, pp. 1109–1115. doi:10.1109/CDC.1984.272186.
- [3] Du, Y. L., Xia, Q. L., and Guo, T., "Study on stability of strapdown seeker scale factor error parasitical loop," *2010 International Conference on Computer, Mechatronics, Control and Electronic Engineering, CMCE 2010*, Vol. 6, 2010, pp. 55–58. doi:10.1109/CMCE.2010.5609905.

- [4] Kim, T.-H., Park, B.-G., Kwon, H.-H., Kim, Y.-H., and Tahk, M.-J., “Stability Analysis of Missiles with Strapdown Seeker,” *Journal of the Korean Society for Aeronautical & Space Sciences*, Vol. 39, No. 4, 2011, pp. 332–340. doi: 10.5139/JKSAS.2011.39.4.332.
- [5] Jianmei, S., Gaohua, C., Xianxiang, C., and Lixia, K., “Stability region analysis of the parasitic loop of the semi-strapdown homing seeker,” *Proceedings of the Institution of Mechanical Engineers, Part I: Journal of Systems and Control Engineering*, Vol. 226, No. 4, 2012, pp. 550–562. doi:10.1177/0959651811421710.
- [6] Jianmei, S., Gaohua, C., Lixia, K., and Jianhua, F., “Precision Analysis of the Semi-Strapdown Homing Guided System,” *Journal of Aerospace Engineering*, Vol. 27, No. 1, 2014, pp. 151–167. doi:10.1061/(ASCE)AS.1943-5525.0000218.
- [7] Bai, R., Xia, Q.-L., Du, X., and Lu, T.-Y., “Test of Parasitic Loop Quality of Strapdown Seeker,” *Binggong Xuebao/Acta Armamentarii*, Vol. 38, No. 3, 2017, pp. 494–500. doi:10.3969/j.issn.1000-1093.2017.03.011.
- [8] Bai, R., Xia, Q., and Du, X., “Analysis of the parasitical loop and guidance performance of phased array seeker with platform,” *Xi Tong Gong Cheng Yu Dian Zi Ji Shu/Systems Engineering and Electronics*, Vol. 39, No. 12, 2017, pp. 2765–2771. doi:10.3969/j.issn.1001-506X.2017.12.20.
- [9] Kim, D., Park, W., and Ryoo, C.-K., “Look-Angle-Control Guidance for Missiles with Strapdown Seeker,” *Journal of Institute of Control, Robotics and Systems*, Vol. 19, No. 3, 2013, pp. 275–280. doi:10.5302/J.ICROS.2013.12.1809.
- [10] Lee, C. H., Hyun, C., Lee, J. G., Choi, J. Y., and Sung, S., “A hybrid guidance law for a strapdown seeker to maintain lock-on conditions against high speed targets,” *Journal of Electrical Engineering and Technology*, Vol. 8, No. 1, 2013, pp. 190–196. doi:10.5370/JEET.2013.8.1.190.
- [11] Hong, J.-H., and Ryoo, C.-K., “Compensation of Parasitic Effect in Homing Loop with Strapdown Seeker via PID Control,” *Proceedings of the 11th International Conference on Informatics in Control, Automation and Robotics*, 2014, pp. 711–717. doi:10.5220/0005055907110717.
- [12] Yun, J.-S., Ryoo, C.-K., and Song, T.-L., “Guidance Filter Design Based on Strapdown Seeker and MEMS Sensors,” *Journal of the Korean Society for Aeronautical & Space Sciences*, Vol. 37, 2009, pp. 1002–1009. doi:10.5139/JKSAS.2009.37.10.1002.
- [13] Sun, T., Chu, H., Zhang, B., Jia, H., Guo, L., Zhang, Y., and Zhang, M., “Line-of-Sight Rate Estimation Based on UKF for Strapdown Seeker,” *Mathematical Problems in Engineering*, Vol. 2015, 2015. doi:10.1155/2015/185149.
- [14] Kim, T.-H., Kim, J.-H., and Kim, P., “New Guidance Filter Structure for Homing Missiles with Strapdown IIR Seeker,” *International Journal of Aeronautical and Space Sciences*, Vol. 18, No. 4, 2017, pp. 757–766. doi:10.5139/IJASS.2017.18.4.757.
- [15] Shneydor, N. A., *Missile guidance and pursuit: kinematics, dynamics and control*, Elsevier, 1998, pp. 101–127. doi: 10.1533/9781782420590.47.

- [16] Balakrishnan, S. N., Stansbery, D. T., Evers, J. H., and Cloutier, J. R., "Analytical guidance laws and integrated guidance/autopilot for homing missiles," *Proceedings of IEEE International Conference on Control and Applications*, 1993, pp. 27–32 vol.1. doi:10.1109/CCA.1993.348311.
- [17] Song, T. L., Shin, S. J., and Cho, H., "Impact angle control for planar engagements," *IEEE Transactions on Aerospace and Electronic Systems*, Vol. 35, No. 4, 1999, pp. 1439–1444. doi:10.1109/7.805460.
- [18] Reichert, R. T., "Application of H (infinity) control to missile autopilot design," *Guidance, Navigation and Control Conference*, 1989, p. 3550. doi:10.2514/6.1989-3550.
- [19] Das, A., Garai, T., Mukhopadhyay, S., and Patra, A., "Feedback linearization for a nonlinear skid-to-turn missile model," *First India Annual Conference*, IEEE, 2004, pp. 314–317. doi:10.1109/INDICO.2004.1497762.
- [20] Horton, M., "Autopilots for tactical missiles: An overview," *Proceedings of the Institution of Mechanical Engineers, Part I: Journal of Systems and Control Engineering*, Vol. 209, No. 2, 1995, pp. 127–139. doi:10.1243/PIME_PROC_1995_209_373_02.
- [21] Williams, D., Richman, J., and Friedland, B., "Design of an integrated strapdown guidance and control system for a tactical missile," *Guidance and Control Conference*, 1983, p. 2169. doi:doi.org/10.2514/6.1983-2169.
- [22] Nesline, F. W., and Zarchen, P., "Missile guidance design tradeoffs for high-altitude air defense," *Journal of Guidance, Control, and Dynamics*, Vol. 6, No. 3, 1983, pp. 207–212. doi:10.2514/3.19817.
- [23] Klein, I., and Rusnak, I., "Loop-Shaping Approach to Mitigate Radome Effects in Homing Missiles," *Journal of Guidance, Control, and Dynamics*, Vol. 40, No. 7, 2017, pp. 1789–1795. doi:10.2514/1.G000850.
- [24] Kalata, P., "The tracking index: A generalized parameter for α - β and α - β - γ target trackers," *IEEE Transactions on Aerospace and Electronic Systems*, Vol. AES-20, No. 2, 1984, pp. 174–182. doi:10.1109/CDC.1983.269580.
- [25] Jang, S. A., Ryoo, C. K., Choi, K., and Tahk, M. J., "Guidance algorithms for tactical missiles with strapdown seeker," *Proceedings of the SICE Annual Conference*, Vol. 1, No. 2, 2008, pp. 2616–2619. doi:10.1109/SICE.2008.4655108.
- [26] Dorf, R. C., and Bishop, R. H., *Modern control systems*, Pearson, 2008, pp. 604–607.
- [27] Lin, C.-F., *Modern navigation, guidance, and control processing*, Prentice-Hall, 1991, pp. 100–102.